Journal of Materials Chemistry A

ROYAL SOCIETY OF CHEMISTRY

PAPER

View Article Online
View Journal

Cite this: DOI: 10.1039/d3ta06147g

Multifunctional fluorescent SPIONs display exceptional optical/magnetic contrast and enhanced photoconductivity in interdigitated electrode based photoresponsive devices†

Ashish Tiwari, *[ab] Ayan Debnath,[c] Mohamad G. Moinuddin,[d] Aamir Mushtaq, [e] Anup Singh, [c] Satinder K. Sharma [d] and Jaspreet K. Randhawa *[a]

SPION based multifunctional nanostructures have gained significant attention in multiscale imaging and therapeutic applications. Multistep synthesis and post-synthesis modifications/doping have been extensively used to synthesize such nanostructures; however, single step synthesis and *in situ* surface coating/doping are still challenging and require the development of a robust method. Using a direct synthesis approach, we address this research dilemma by synthesizing nitrogen doped carbon coated core–shell SPIONs along with nitrogen doped carbon dots as a biproduct. This method allows for the creation of two products from a single synthesis as well as *in situ* doping in both products. The synthesized core–shell SPIONs demonstrated unique two-photon absorption, multicolor emission behavior and optical nonlinearity, which are essential for optical and fluorescence imaging applications. Moreover, by customizing the core shape and shell surface coating, core–shell SPIONs demonstrated high saturation magnetization, increased magnetic contrast, and high T2 relaxivity ($R = 156\ mM^{-1}\ s^{-1}$). Additionally, in order to assess the efficacy of photoinduced conduction, we constructed an interdigitated electrode device utilizing these SPIONs. The generation of photocurrent was evaluated across various illumination conditions. The device demonstrated exceptional photoconductivity, as evidenced by the observed photo-to-dark current ratio (ION-IDark/IDark) of 7.53 and 6.64 under green and red laser illumination, respectively. The photocurrent study measured the rise and fall times of device response to be 93/281 milliseconds under green laser illumination determining the strong applicability of SPIONs in device applications. The enhanced photoelectronic capabilities may be attributed to the utilization of carbon shells as active light harvesting sites and nitrogen doping as charge donors within the core–shell architecture. The current study elucidates a synthesis technique for the production of multifunctional fluorescent SPIONs and reveals their immense potential for applications in photoresponsive devices and multiscale imaging.

Received 10th October 2023
Accepted 18th December 2023

DOI: 10.1039/d3ta06147g

rsc.li/materials-a

1 Introduction

Biomedical researchers are intrigued by the multifunctionality of superparamagnetic iron oxide nanoparticles (SPIONs). These nanostructures have proven useful in a variety of applications, including magnetic resonance imaging, drug delivery and flexible bioelectronic devices.[1–3] Several studies have reported the synthesis of these nanoarchitectures using a multistep fabrication process and hybrid approaches to achieve optical[4–6] and magnetic properties.[7,8] As an illustration, the synthesis of core–shell supernanoparticles with a fluorescent coating of silica was carried out by a multistep method using SPIONs and quantum dots.[7] Similarly, magneto-fluorescent nanohybrid quantum dots/quantum rods (QDQRs) were fabricated in multistep synthesis.[9] Fluorescent-tagged multifunctional core–shell nanoparticles in post-synthesis modification were reported.[10]

[a]School of Mechanical and Materials Engineering, Indian Institute of Technology Mandi, Himachal Pradesh, 175005, India. E-mail: ashishtiwari111@outlook.com; ashish.larpm@gmail.com; ashisht@campus.technion.ac.il; jaspreet@iitmandi.ac.in

[b]Faculty of Biomedical Engineering, Technion-Israel Institute of Technology, Haifa, 3200003, Israel

[c]Center for BioMedical Engineering, Indian Institute of Technology Delhi, New Delhi, 110016, India. E-mail: Anup.Singh@cbme.iitd.ac.in; ayan.newton@gmail.com

[d]School Computing and Electrical Engineering, Indian Institute of Technology Mandi, Himachal Pradesh, 175005, India. E-mail: moin.ahmad111@gmail.com; satinder@iitmandi.ac.in

[e]Department of Materials Science and Engineering, Ohio State University, Ohio 43210, USA. E-mail: mushtaq.11@osu.edu

† Electronic supplementary information (ESI) available: Materials and methods, table of content, NMR spectra, emission spectra, DLS analysis and device fabrication methods. See DOI: https://doi.org/10.1039/d3ta06147g

Furthermore, a combination of methods was used to produce polymer-coated superparamagnetic iron oxide nanoparticles (SPIONs) with magnetic and luminous properties.[11] Although these methods produced fluorescent SPIONs, they are constrained by concerns such as multistep synthesis, post-synthesis modifications, toxicity, and photobleaching. A hybrid strategy of merging two synthesized materials in a single step or coating of a shell over the synthesized core material was reported.[12] Few examples of single step synthesis reported metal oxide core–shell structures but most of them consisted of a metal and metal oxide core–shell or composite structure.[13–16] SPIONs' spherical core–shell form and synergistic magneto-fluorescence characteristics have rarely been observed. Furthermore, there is no existing literature on the combination of a magnetite core, core–shell morphology and doping processes. Additionally, the two-product idea, which involves synthesizing both components in a single step, has not been established. Hence, it is imperative to devise a single-step synthesis technique.

The structural alterations have an impact on the magnetic susceptibility of SPION[17,18] resulting in superior magnetic resonance contrast.[19,20] It is preferable to dope or coat SPIONs with metallic or nonmetallic elements in order to enable fluorescence behaviour.[20,21] Carbogenic species have fluorescence properties and can be effectively combined with SPIONs to induce optical activity. For instance, carbon dots,[22,23] doped carbon dots[24] and carbon quantum dots[25] demonstrate absorption characteristics in the visible and near-infrared regions, thereby broadening their potential utility in the fields of fluorescence and two-photon fluorescence imaging. In a comparable way, nitrogen as a potent dopant[26] also contributes to improve optical and electrical characteristics with minimal disruption to the crystal lattice structure[27] and introduces defective sites into structures.[28] Consequently, *in situ* carbogenic material's coating and nitrogen doping can enhance the optical response of SPIONs in multiscale magneto-fluorescence imaging.

Utilizing multifunctional heterostructures has been a recent focus in electronic device developments, especially in the domains such bioelectronics[3] and flexible electronics.[29] Although organic and inorganic photodetectors show excellent light-sensing performance and tunable optoelectronic properties, there are still challenges in fabricating these devices such as lack of ease of processing, mechanical flexibility and multifunctionality. Enhanced sensitivity in light detection has been achieved in modern photodevices through the optimization of two critical factors: high responsivity and low dark current. An illustration can be provided by the graphene–polymer hybrid electrode, which exhibited both rise and fall times of 1.58 ms and 1.57 ms.[30] Similarly, a hybrid graphene–metal oxide based photodevice showed a response time of less than 30 ms.[31] Due to the need for rapid response and high sensitivity, interdigitated electrode-based photoresponsive devices employing optically active SPIONs have been developed. In addition to enhanced photoconductivity, it is anticipated that these devices will perform more efficiently in multiscale imaging applications.

Hence, by employing the principle of integrating magnetic and optical characteristics and including *in situ* doping, we have introduced an innovative single-step synthesis method of fabricating fluorescent SPIONs and successfully produced two unique nanoscale materials. The synthesized nitrogen-doped carbon-coated ultrasmall superparamagnetic iron oxide core–shell nanoparticles (SPIONs) and the nitrogen-doped carbon dot nanoparticles (NCDs) were subjected to comprehensive quantitative and qualitative analysis to assess their exceptional physicochemical features. In addition, the magnetic separation and column chromatography (CC)-based purification phases resulted in two products with distinct morphologies and properties. In this study, SPIONs exhibited a uniform core–shell morphology with a nanocrystal magnetic core and a carbon shell, multicolor emission, two photon absorption, nonlinear optical properties, superior magnetic resonance imaging contrast, and photoinduced conduction behavior under visible light illumination. The μ-interdigitated photoelectrodes incorporating manufactured SPIONs exhibited a prompt response to the incidence of light and generated a photocurrent. The findings of the photolithography-driven device fabrication demonstrate the promising potential of these photoelectrodes for integration into optoelectronic devices.

2 Results

2.1 One step synthesis method, magnetic separation, and nanoparticle purification

To synthesize, separate, and purify two distinct nanoscale products, we used a one-step hydrothermal synthesis method and magnetic separation to obtain a brown precipitate and a black supernatant, as depicted in Scheme 1. The brown precipitate underwent multiple washes and was then dried in a vacuum oven overnight at 40 °C. This process ensured the removal of any impurities and yielded nitrogen doped carbon coated core–shell SPIONs (SPIONs). On the other hand, the black supernatant was purified by silica gel column chromatography to get nitrogen doped carbon dots (NCDs). The successful incorporation of nitrogen into both core–shell SPIONs and NCDs was attributed to the nitrogen-based precursor material during synthesis.

In our previous work, we have reported carbon coated core–shell SPIONs[32] and optimized the carbon shell thickness. The carbon coating and tuning of shell thickness governed the magneto-fluorescence properties, which was evident and established by synthesizing various core–shell morphology tuned carbon coated SPIONs.[33] These materials showed superior MR imaging, bioimaging, fluorescence sensing, hyperthermia and targeted drug delivery.[34–37] Extending the possibility of core–shell SPIONs in opto-electronic applications, we attempted to incorporate nitrogen in core–shell SPIONs using our established protocol. We used a nitrogen-based precursor and the synthesized nitrogen doped carbon coated core–shell SPIONs by optimizing the precursor concentration as detailed in Table S1 in the ESI.† As stated elsewhere, the method produced nitrogen doped carbon dots as a product from synthesis. The outlined methodology stands unique in terms of single step synthesis and *in situ* nitrogen doping and carbon coating avoiding post-synthesis modifications/coating/doping to accomplish uniform morphology and distinct

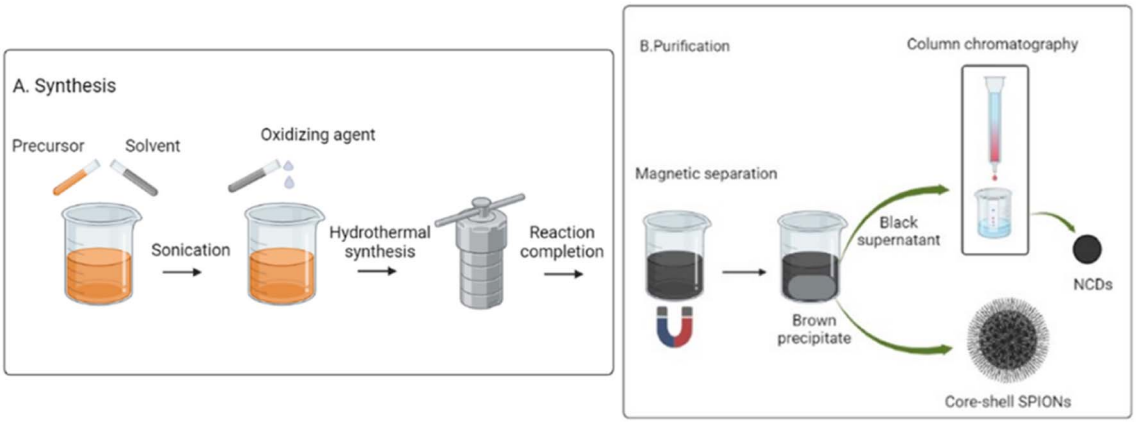

Scheme 1 Schematic representation of (A) the one step synthesis method and (B) magnetic separation and purification of the synthesized products.

physiochemical properties in core-shell SPIONs. Fig. S1 in the ESI† displays FESEM imaging results of solely prepared core–shell SPIONs for comparison.

2.2 Uniform morphology, phase pure crystallinity and multifunctional surface functionality govern distinct properties in core–shell SPIONs

Fig. 1a shows the transmission electron microscopy (TEM) image, clearly showing the distinguishable magnetic core composed of ultrasmall magnetite nanocrystals and a carbon shell within a uniform morphology. The magnetic core consisted of small magnetite nanocrystals and coated with a carbon shell, resulting in a core–shell structure with an average particle size of ~250 nm. The high resolution transmission electron microscopy (HR-TEM) image in Fig. 1b confirms the presence of ultrasmall magnetite nanocrystals in the core region with an average size of ~5 nm and carbon coating of ~20 nm in the shell region. The carbon coating not only determines the spherical morphology but also plays a crucial role in stabilizing and controlling thermodynamic self-aggregation of ultrasmall magnetite nanocrystals during the formation of a uniform core–shell structure. The ultrasmall magnetite nanocrystals induce superparamagnetism and high susceptibility under externally applied magnetic fields.[38] The selected area electron diffraction (SAED) pattern in Fig. 1c displayed the diffraction rings for the magnetite phase of iron oxide well matched with X-ray diffraction (XRD) results. The field-emission scanning electron microscopy (FESEM) image in Fig. 1d showed the uniform morphology of core–shell SPIONs. Elemental mapping to confirm the presence of nitrogen *via* scanning transmission electron microscopy-high angle annular dark-field (STEM-HAADF) imaging in Fig. 1e–j shows the overlay mapping image and distinct element images of iron (g), nitrogen (h), oxygen (i), and carbon (j), respectively. Electron microscopy results validate the nitrogen doping, the presence of the magnetic core, and the carbon shell in core–shell SPIONs.

XRD measurements were done to identify phase crystallinity. Fig. 2a displays the diffraction pattern with distinct peaks at various 2θ values, corresponding to the reflection of crystal planes (111), (022), (220), (311), (400), (422), (511), (440), and (533). These peaks confirm the magnetite phase of iron oxide, which matches well with the Standard International Centre for Diffraction Data sample database (JCPDS card no. 01-1111). Additionally, a small peak at a 2θ of 24° indicates the presence of amorphous carbon in core–shell SPIONs. Raman spectroscopy results further confirmed the magnetite phase of iron oxide. Fig. 2b shows Raman bands at 215, 272, 391, 514, and 690 cm^{-1}, corresponding to different

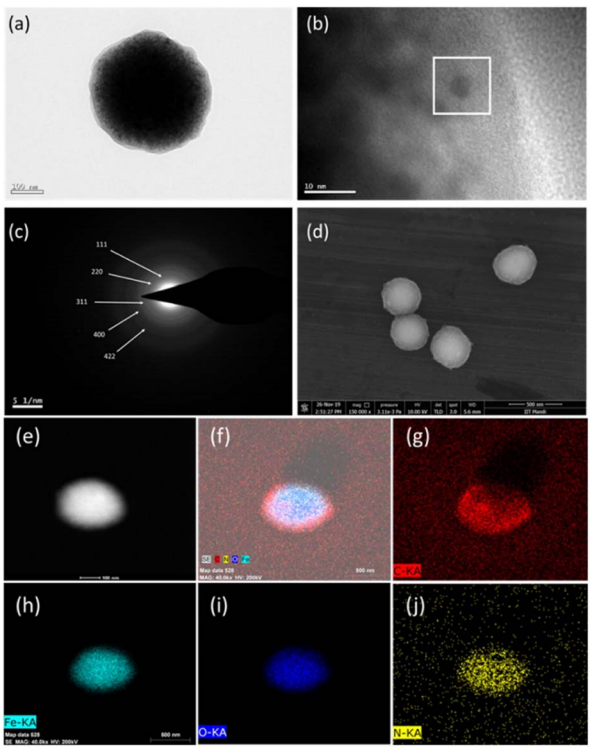

Fig. 1 (a) TEM image, (b) HR-TEM image, (c) SAED pattern and (d) FESEM image of core–shell SPIONs, respectively. STEM-HAADF image (e) along with the color mapping overlay image (f) and respective elemental images: (g) carbon, (h) iron, (i) oxygen and (j) nitrogen, respectively (scale bar: (a) 100 nm and (b) 10 nm, (c) 5^{-1} nm, (d) 500 nm and (e–j) 100 nm, respectively).

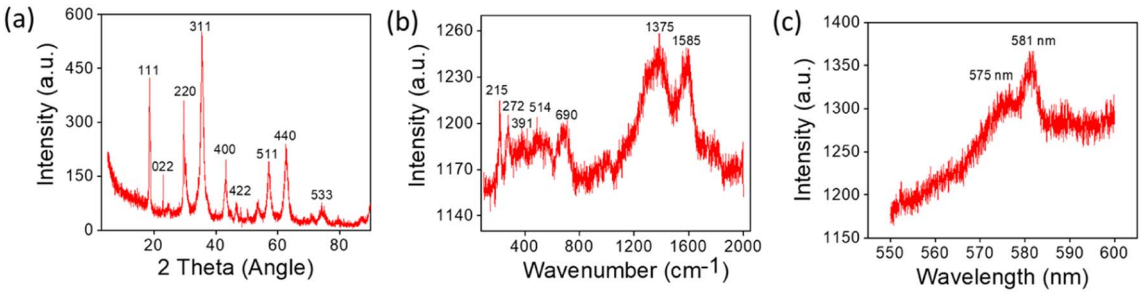

Fig. 2 (a) XRD spectra, (b) Raman spectra and (c) PL Raman spectra of core–shell SPIONs, respectively.

bending modes of magnetite. The bands at 1375 and 1585 cm^{-1} are attributed to the disordered sp^3 and graphitic sp^2 domains of carbon atoms in the shell. The relatively lower intensity ratio of D and G bands suggests an amorphous phase of carbon and dominant disordered regions due to nitrogen doping, indicating the presence of surface defects. Photoluminescence is a phenomenon in which a material emits light after absorbing photons. The optical behavior of the material was investigated using Raman spectroscopy. In Fig. 2c, two distinct peaks are detected at 575 and 581 cm^{-1}, providing confirmation of the luminescence characteristics that emphasize the potential optical qualities present in core–shell superparamagnetic iron oxide nanoparticles (SPIONs).

X-ray photoelectron spectroscopy (XPS) studies were performed to evaluate functional group analysis and elemental oxidation states. Fig. 3a presents full survey XPS spectra, which confirm the presence of iron, oxygen, carbon, and nitrogen in core–shell SPIONs. The high-resolution deconvoluted XPS spectra of Fe 2p in Fig. 3b exhibit four peaks at binding energies of 710.35, 712.71, 723.62, and 725.71 eV for Fe $2p_{3/2}$ and Fe $2p_{1/2}$, along with one shake-up satellite peak at 717.52 eV. These peaks are attributed to the Fe^{3+} and Fe^{2+} oxidation states of iron and confirm the magnetite phase. In Fig. 3c, the deconvoluted O 1s spectra display four peaks at binding energies of 530.12, 531.57, 532.47, and 533.61 eV, corresponding to Fe–O, C=O, N–C=O, and O–C–O functional groups, respectively. The high-resolution C 1s XPS spectra in Fig. 3d exhibit four peaks centered at binding energies of 284.81, 285.76, 286.35, and 288.39 eV, representing C=C, C=N, C–O–C, and C=O functional groups, respectively. Furthermore, in Fig. 3e, the high-resolution deconvoluted N 1s spectra display two peaks at binding energies of 399.92 and 401.52 eV, which can be attributed to the presence of C–NH and N–C=O or N–Fe–O functional species, respectively. XPS results confirm the magnetite phase of iron oxide, abundant surface carbonyl and hydroxyl groups, and nitrogen in core–shell SPIONs.[26] These findings are further supported by the Fourier transform infrared (FTIR) results. Fig. 3f shows vibrational peaks corresponding to functional groups and metal oxide linkages present in core–shell SPIONs. Two peaks observed at 3340 and 2930 cm^{-1} can be attributed to O–H and N–H functional group species. Furthermore, vibrational peaks around 1708, 1610, 1320, and 820 cm^{-1} correspond to C=O, C=C, C–O–C, and C–OH functional groups, respectively. These peaks indicate the presence of various surface carbonyls and hydroxyl groups, which play a crucial role in excellent colloidal stability and dispersibility. Additionally, a peak observed at 560 cm^{-1} corresponds to the metal oxide linkage for magnetite in core–shell SPIONs. To assess colloidal stability and surface charge, dynamic light scattering tests were performed. As illustrated in Fig. S2 in the ESI,† the hydrodynamic dimension in aqueous medium was determined to be approximately 350 nm. Surface charge was determined using zeta potential studies, as shown in Fig. S3 in the ESI,† producing a value of 10 mV in aqueous solution. This confirms the stabilized surface of core–shell SPIONs due to the presence of nitrogen- and oxygen-based functional groups.

2.3 Carbon coating enables multicolor emission and two-photon absorption in core–shell SPIONs

Fig. 4a shows a broad absorption peak ranging from 800 to 200 nm in the UV-vis spectrum. Solid state absorption spectra were recorded to calculate the band gap of core–shell SPIONs, which was found to be ~2.25 eV (Fig. 4b). This behavior resembles the characteristic absorption of carbogenic structures and is due to the presence of the carbon coating in the shell structure. Fluorescence spectroscopic studies were done to investigate their emission behavior. Since the absorption spectra of SPIONs displayed a broad peak in the UV-visible region, the choice of the excitation wavelength was based on the highest emission observed in the fluorescence spectra, as shown in Fig. 4a. The SPIONs exhibited excitation-based emission spectra, which was also a novel observation. The excitation peak was measured at 360 nm, as shown in Fig. 4c. Fig. 4d depicts an excitation-dependent emission spectrum (400–650 nm) that showed the presence of intrinsic fluorescence in core–shell SPIONs. The emission patterns were found to exhibit characteristic indications of a carbogenic composition.[39] The inherent emission behavior can be attributed to surface energy traps, and emission originates from rich carboxyl and hydroxyl groups as reported for carbon nanostructures.[40] Fig. S4 in the ESI† illustrates emission behavior in different pH media with no significant change in intensity, which suggests their potential optical imaging applications in dispersed media such as cell lysates and cell cytoplasm, enabling intracellular imaging of biomolecules.

The Z-scan methodology presents a direct approach for quantifying the phase alteration experienced by a laser beam while traversing a nonlinear medium. This technique enables the determination of both the sign and amount of the phase

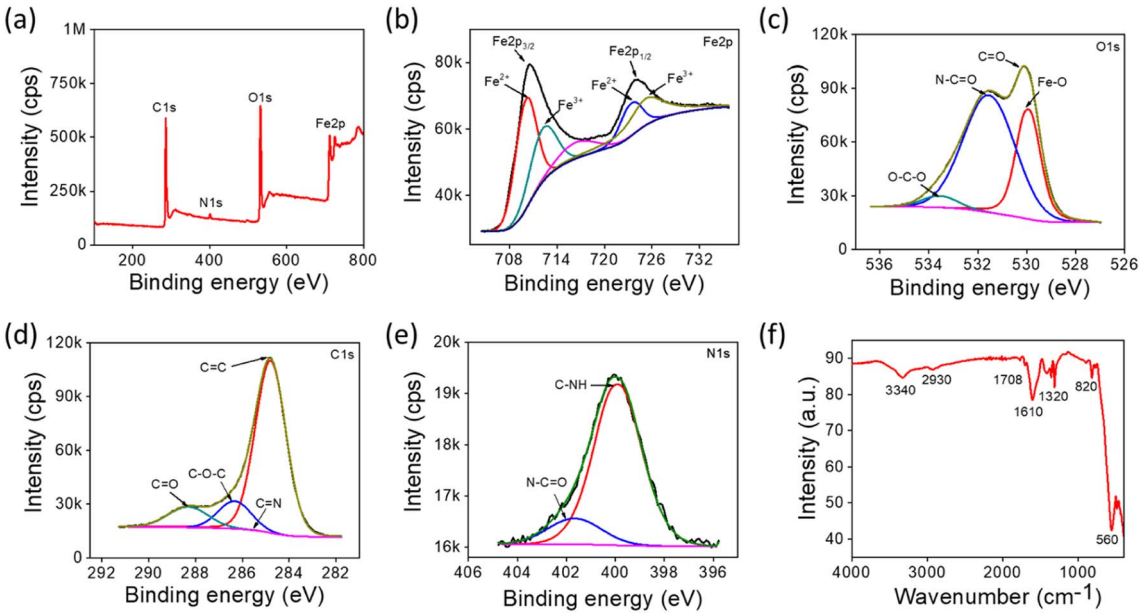

Fig. 3 (a) Full survey XPS spectra. High resolution deconvoluted XPS spectra of (b) iron, (c) oxygen, (d) carbon and (e) nitrogen, respectively and (f) FTIR spectra of core–shell SPIONs.

shift, which are intimately linked to the fluctuations in the refractive index of the material. Furthermore, the Z-scan technique measures alterations in transmission that arise from nonlinear absorption, a phenomenon closely linked to the absorption coefficient. In order to validate the nonlinear optical characteristics, a scan measurement was conducted subsequent to the drop casting of core–shell SPIONs onto a glass substrate. In Fig. 5a the Z-scan results show a transmittance loss of around 0.92 and 0.78 for two distinct laser illumination powers, 212 mW and 252 mW, respectively. Fig. 5b depicts PL intensity measured at 560 nm after illumination with an excitation wavelength of 800 nm. The emission spectra were recorded at two distinct laser illumination powers, specifically 212 and 252 mW. The results indicate that core–shell SPIONs possess intrinsic optical nonlinearity and two-photon absorption, neither of which have been extensively documented in prior

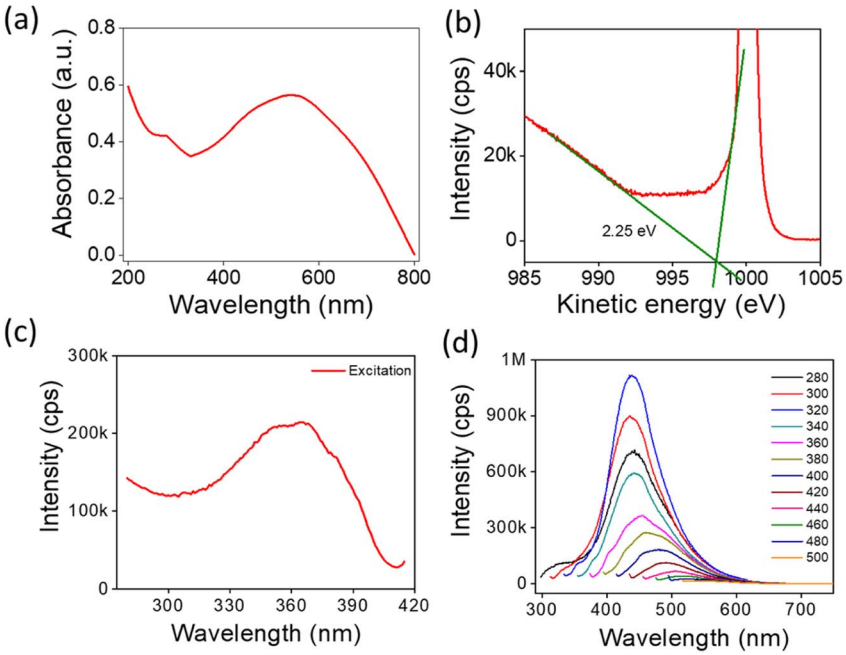

Fig. 4 (a) Absorption spectra, (b) optical band gap estimation, (c) excitation spectra and (d) excitation dependent emission spectra of core–shell SPIONs, respectively.

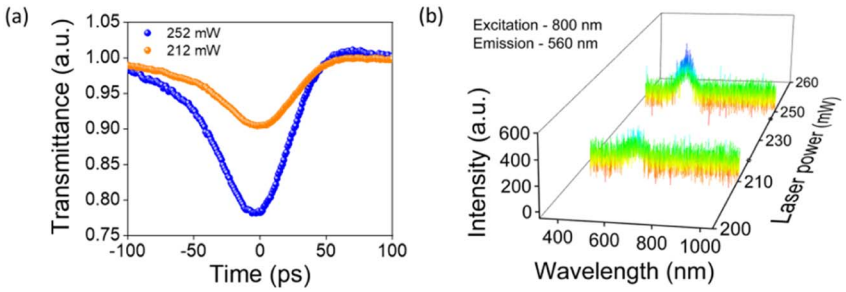

Fig. 5 (a) Z-scan measurement spectra and (b) PL emission spectra of core–shell SPIONs at two laser powers, respectively (excitation – 800 nm and PL emission – 560 nm) (laser power – 212 and 252 mW).

research. The potential for the development of innovative applications of core–shell SPIONs in the domain of infrared bioimaging is substantial, as suggested by these observations. The work in greater detail will be examined afterward.

2.4 Ultrasmall magnetite nanoparticles bring about superior magnetic susceptibility and high relaxivity contrast in MR imaging

A superconducting quantum interference device-vibrating sample magnetometer (SQUID-VSM) equipment was used to evaluate the magnetic susceptibility of core–shell SPIONs. Fig. 6a shows the magnetic hysteresis (M–H) curve recorded at 300 K under a magnetic field of 4 T. We estimated a saturation magnetization (Ms) of 42.92 emu g^{-1}, remanent magnetization (Mr) of 1.12 emu g^{-1}, and coercivity (Hc) of 43.40 gauss. The minimum remnant magnetization and low coercivity value establish superparamagnetism in core–shell SPIONs.[38] Temperature-dependent field-cooled (FC) and zero-field-cooled (ZFC) magnetization curves, presented in Fig. 6b, showed a single transition separating FC and ZFC curves at 240 K, confirming superparamagnetism at room temperature. The observed superparamagnetic nature may be attributed to ultrasmall magnetite nanoparticles (~5 nm) in the magnetic core. The inherent magnetic characteristics and colloidal dispersibility of core–shell SPIONs in aqueous media were examined. After attaining equal dispersion, an experiment was carried out in which a magnet was placed in close proximity to the scattered material. As a result, there was a noticeable phenomenon of rapid aggregation towards the magnet. Nonetheless, after the magnet was removed, a minor form of agitation caused the re-dispersion of colloidal particles. Magnetic resonance (MR) imaging relies heavily on the fast magnetic response and remarkable colloidal dispersibility in aqueous fluids. The presence of a carbon coating as well as an abundance of carbonyl, hydroxyl, and nitrogen groups on the surface of core–shell SPIONs improves water molecule accessibility to the sample surface. As a result, the SPIONs have better dispersibility and great magnetic susceptibility.

Furthermore, we performed MR imaging to evaluate the potential of core–shell SPIONs as a contrast agent. SPIONs are commonly used as T2 contrast agents due to their ability to reduce the signal intensity by dephasing the transverse magnetization, leading to a decrease in transverse relaxation time T2 and producing negative contrast. To validate this, phantoms were prepared using agarose gel as a tissue mimic medium, with different concentrations of core–shell SPIONs. In Fig. 6c, the phantom MR color map showed a decrease in relaxation time (red color to blue color) with increasing concentration of core–shell SPIONs. A decrease in MR signal intensity resulted in enhanced negative contrast, or darkening, compared to pure agarose gel and when core–shell SPIONs were present. The plot in Fig. 6d illustrates the relationship between the relaxation rate (1/T2) and Fe concentration in core–shell SPIONs (ranging from 0.01 to 0.10 mM). Through linear fitting of the plot, the relaxivity value ($r2$) was calculated to be 156 mM^{-1} s^{-1}. The measured relaxivity was determined to be higher than that of contrast agents available in the market and those reported in the literature (Table S2 in the ESI†).[41,42] This suggests that core–shell SPIONs can be a good T2-weighted negative contrast agent for non-invasive MR imaging in disease diagnosis.

2.5 Magnetic imaging confirms superparamagnetism and local magnetic domains in single core–shell SPIONs

Magnetic force microscopy (MFM), scanning associated atomic force microscopy, uses a magnetic probe which interacts with magnetic fields in close proximity to a sample surface. MFM detects nanoscale magnetic interactions, *i.e.*, local magnetic domains by measuring magnetic probe deflections caused by the magnetic properties of the sample surface. We first prepared a pallet of core–shell SPIONs and then performed MFM scanning to acquire magnetic phase images. The scanning was done at a height of 50 nm between the probe tip and sample surface on applying a magnetic field of 500 G. Fig. 7a–d present the images of magnetic regions on the sample surface, along with phase shift, height, and amplitude values. The determined phase contrast was 4.1 radian, with a magnetic angle of 308.6 m° and an amplitude of 841.3 μV. Multiple scans with adjustments in the lift height, local magnetic domain and amplitudes were mapped against the magnetized probe. The negative values in the magnetic phase supported the superparamagnetic behavior of SPIONs and the presence of local magnetic domains in the mapped region.[43]

Furthermore, we decided to map the local magnetic domains of single SPIONs. To achieve this, samples were prepared by spin coating of a single layer of SPIONs on

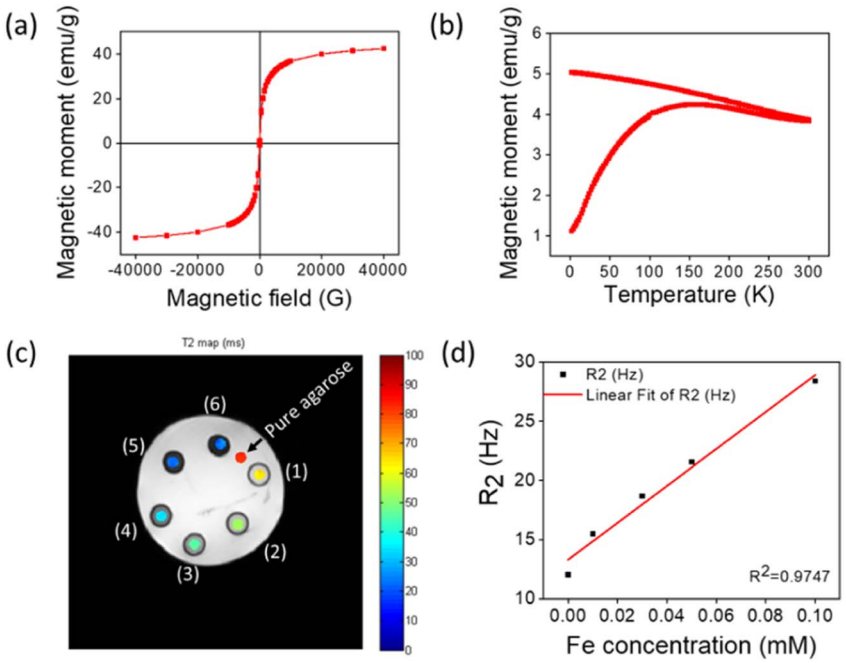

Fig. 6 (a) M–H magnetization curve and (b) temperature-based magnetization FC and ZFC curve of core–shell SPIONs, respectively. (c) T2-weighted color overlaid map image. Numbers (1 to 6) in (c) indicate regions corresponding to small phantom tubes with different concentrations of sample. (d) Plot of *R*2 or 1/T2 *vs.* Fe concentration in the sample (0.01–0.10 mM). The red line in the plot (d) represents a linear fit of the given values. Relaxivity was estimated from the slope of the linear fitted graph. MR imaging was performed on a 3T medical MR scanner.

a silicon dioxide substrate. MFM scanning was performed on a single SPION nanoparticle. Fig. 8a–d display the phase contrast image, which confirms local magnetic domains on the sample surface. The negative values in the magnetic phase image corroborated superparamagnetic behavior and validated that single SPIONs are nanoscale magnetic domains.[44] Understanding the magnetic behavior of SPIONs at the single-particle level is essential for biomolecule sensing, magnetic particle imaging, magnetic hyperthermia, identifying ferritin proteins, and classifying magnetic nanoparticle-labeled cells.[45]

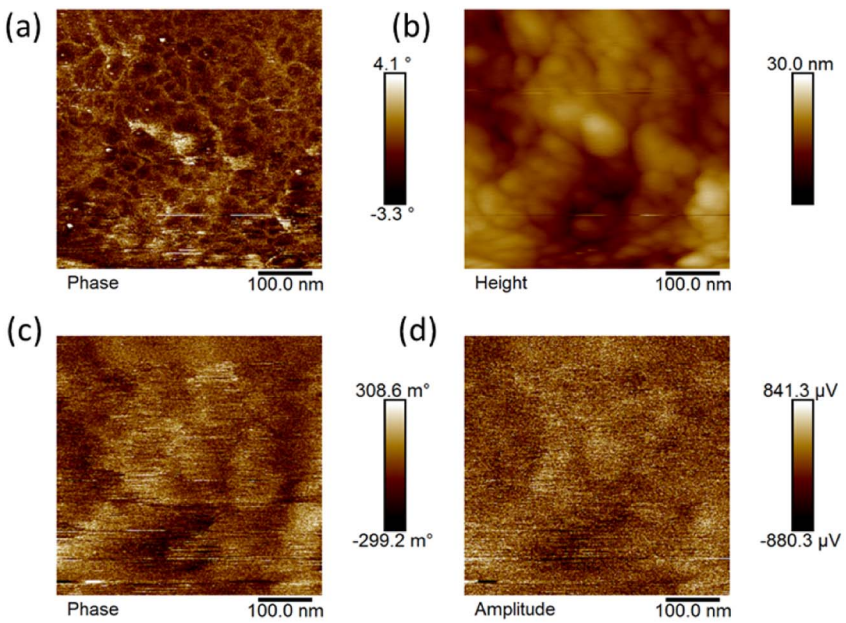

Fig. 7 MFM imaging of a core–shell SPION pallet well patterned on the substrate. (a) Phase contrast image, (b) topological height image, (c) phase contrast image and (d) magnetic signal amplitude images as imaged from MFM scanning in AFM microscopy with the magnetized tip.

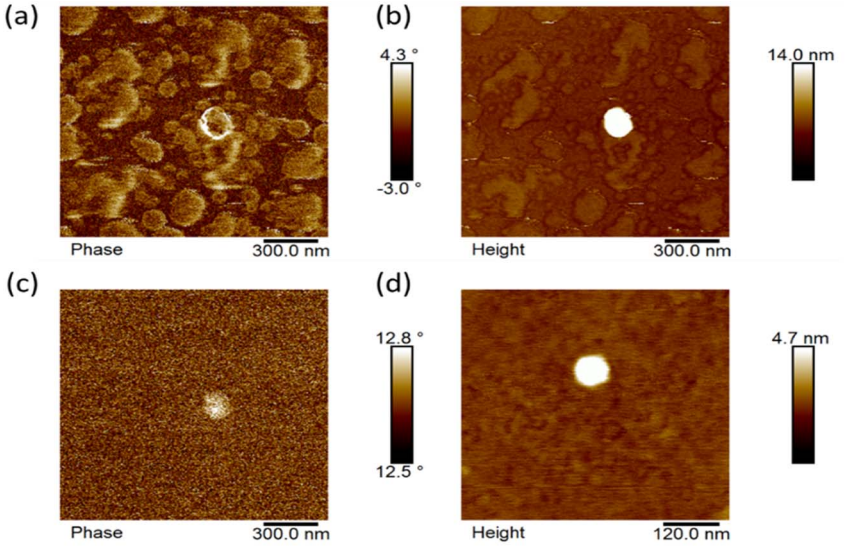

Fig. 8 MFM imaging analysis of a single particle of core–shell SPIONs patterned on a silicon substrate: (a) electrostatic image at a height of 50 nm, (b) topological height image, (c) standard MFM image of single core–shell SPIONs at 500 gauss and (d) topographical AFM image of single core–shell SPIONs, respectively.

2.6 Core–shell SPIONs are biocompatible and show multicolor emission in confocal imaging

We further evaluated the cytotoxicity of core–shell SPIONs using MTT assays on two cancer cell lines: SH-SY5Y neuroblastoma and HT-29 human colorectal adenocarcinoma cells. The cell viability experiments were conducted using various concentrations of sample ranging from 0 to 50 μg ml^{-1}. The cell viability experiments demonstrated significant biocompatibility up to a concentration of 50 μg ml^{-1}. Fig. 9a–d present the dose-dependent cell viability results for both the SH-SY5Y neuroblastoma and HT-29 human colorectal adenocarcinoma cells for 24 and 48 hours, respectively. The cell viability was found to be over 80% even at higher concentrations against both cell lines at both time points. These results indicate that core–shell SPIONs are biocompatible and show great potential to be used in optical bioimaging and cellular internalization studies.

Confocal microscopic imaging revealed a prominent cellular internalization and displayed multicolor emission of core–shell SPIONs. Fig. 10 demonstrates cellular uptake in two cancer cell lines: SH-SY5Y neuroblastoma and HT-29 human colorectal adenocarcinoma cells. In the fluorescence study, the cancer cells were incubated with SPIONs at a concentration of 10 μg ml^{-1}. Imaging samples were prepared on glass slides following the recommended protocol. The results showed multicolor fluorescence from the cell cytoplasm, showing the great efficacy of SPION uptake. The findings imply that SPIONs could be useful as nanocarriers for the targeted delivery of certain biomolecules in cancer therapy.

2.7 High photoconductivity and rapid photo-switching in μ-IDE-Pt/SPION electrode based photoresponsive devices

We further studied the potential of the prepared μ-IDE-Pt/SPION heterostructures in photoresponsive devices. Scheme 2 shows the graphical representation of the photoresponsive device developed using photolithography. The photoelectrodes were prepared by patterning them on silicon dioxide substrates in a sequential lift-off process with a photoresist followed by spin coating of core–shell SPIONs.

Fig. 11a illustrates a non-linear current density plot as voltage increases. This non-linear behavior indicates field-assisted enhanced carrier conduction across the electrode. The increased carrier conduction can be attributed to Fowler–Nordheim tunnelling of the HUMO (highest occupied molecular orbital) electrons under the influence of an electric field.[46] It is noteworthy that uniformly coated core–shell SPIONs contribute to symmetric current–voltage characteristics (*I–V*) in a bilaterally symmetric manner. This symmetric behavior can be advantageous for the integration of such device structures in system-on-chip configurations.[47,48] Additionally, the conductance *versus* voltage characteristics also exhibit a non-linear behavior and reach saturation at approximately 7.8 V, as shown in Fig. 11a (inset). This behavior further emphasizes the unique electrical properties of the μ-IDE Pt/SPION heterostructure in photoresponsive devices. In the study, the fabricated μ-IDE-Pt/SPION heterostructures were subjected to green and red illumination, resulting in a one-order variation in device current. The photoresponsive devices based on μ-IDE-Pt/SPIONs exhibited rapid optical to current responsiveness and a substantial photo to dark current ratio. The study on photoinduced current investigated the rise and fall times of the device's reaction, which were found to be 93/281 milliseconds when exposed to a green laser. This finding suggests that the device has significant potential for use in printed electronic health monitoring systems. In contrast, non-communicable diseases have exhibited a range of desirable characteristics, including

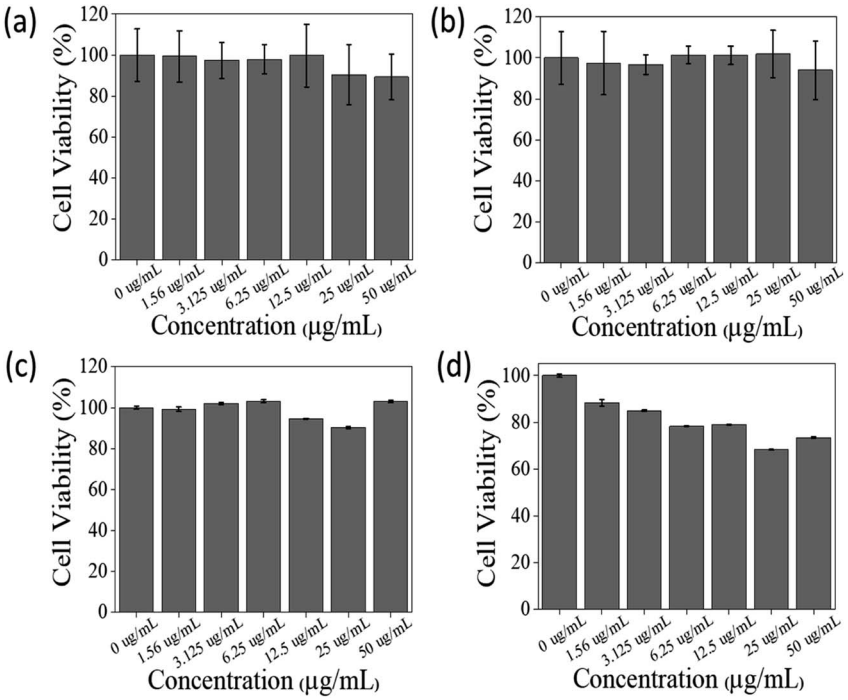

Fig. 9 Cell viability experimental studies evaluated SH-SY5Y neuroblastoma and HT-29 human colorectal adenocarcinoma cells. (a and b) Bar chart and error bars for percentage cell viability in SH-SY5Y neuroblastoma cells for 24 and 48 hours (c and d). Bar chart and error bars for percentage cell viability in HT-29 colorectal adenocarcinoma cells for 24 and 48 hours, respectively (data are mean ± SD) (sample concertation = 0–50 μg ml^{-1}).

multifunctionality, biocompatibility, multicolor emission, and significant potential for utilization in cellular imaging within the realm of biomedical applications. Moreover, this research offers abundant prospects for investigating the synthesis of nanoscale materials using a single step process, as well as achieving a high throughput yield in their manufacture. In the future, the utilization of multifunctional core–shell superparamagnetic iron oxide nanoparticles (SPIONs) as illustrated in this study could hold significant value in the development of interdigitated optoelectronic devices aimed at monitoring human health, respectively (Fig. 11b). These ratios indicate the sensitivity of the fabricated device to light, with a higher ratio corresponding to a higher sensitivity. The comparison table in Fig. 11c provides additional insights into the device performance under laser illumination. It shows the rise and fall times of device response, which were measured to be 93/281 milliseconds and 1570/1055 milliseconds for green and red illumination, respectively. The above-mentioned timings indicate the speed at which the current of the device reacts to a light stimulus. In core–shell SPIONs, the increased sensitivity and quicker rise time observed in green light can be attributed to the existence of electron capture sites on the functionalized surface of the carbon shell. Different types of lighting can cause sensitivity in these trap locations. The resonance between the incident light and the bound electron in the SPIONs, which have a bandgap in the range of 532 nm, provides additional support for the greater sensitivity observed under green light illumination. Fig. 11d illustrates the resonance effect. These results demonstrate the photoresponsive device applications of the fabricated μ-IDE-Pt/SPION heterostructure.

2.8 Purification of the supernatant *via* column chromatography produced nitrogen doped carbon dots (NCDs) as a reaction byproduct

After the synthesis and once we collected the core–shell SPIONs from the reaction *via* magnetic separation, we utilized the supernatant and subjected it to purification *via* column chromatography (Scheme 1). Typically, the obtained supernatant was collected with caution and subjected to rotary evaporation, resulting in the formation of a thick liquid. Subsequently, purification was carried out using column chromatography, employing dichloromethane (DCM) and hexane at different ratios, leading to the isolation of the desired products with a DCM–hexane composition of 70%. Column chromatography purification of NCDs was performed using silica gel (mesh size 60–120) following a method similar to a previously described one.[49] The yield of NCDs was calculated to be 15.45%. The purified NCDs were subjected to ^{1}HNMR studies in $CDCl_3$ solvent to get information about the protons associated in the structure. In Fig. S5 (ESI),† the ^{1}H NMR spectra of the purified NCD structure exhibit distinct signals corresponding to the protons associated with the surface hydroxyl and carbonyl groups. The presence of these signals confirms the successful purification of the NCDs, and the spectra indicate the structural integrity of the carbon dot.[49] We used purified NCDs for further characterization and studies.

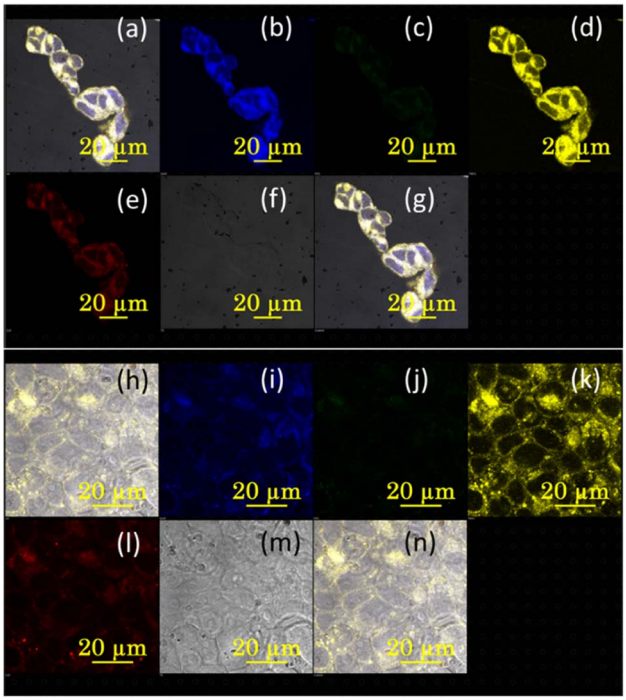

Fig. 10 Confocal microscopy images of core–shell SPIONs against two cancer cell lines under the illumination of different laser channels to observe multicolor behavior in the sample. (a–g) Confocal imaging of the SH-SY5Y neuroblastoma cell line showing the overlay image (a), DAPI channel (b), FITC channel (c), TRITC channel (d), CY5 channel (e), bright field image (f) and overlay of all the channels (g), respectively. (h–n) Confocal imaging of the HT-29 human colorectal adenocarcinoma cell line showing the overlay image (h), DAPI channel (i), FITC channel (j), TRITC channel (k), CY5 channel (l), bright field image (m) and overlay of all the channels (n) respectively (DAPI–blue, FITC–green, TRITC–yellow and CY5–red) (scale bar: 20 μm).

2.9 NCDs are small and semi-crystalline in nature and possess high surface functionality

The transmission electron microscopy (TEM) image in Fig. 12a reveals the spherical morphology of nitrogen doped carbogenic nanodots (NCDs) with a particle size of ~5 nm. The SAED pattern (Fig. 12b) also verified the hexagon pattern and graphitic nature of carbon dots. The small size of NCDs is significant for their potential applications in bioimaging. Fig. 12c presents the XRD pattern of NCDs, exhibiting a distinctive diffraction peak at a 2-theta position of 24°, which corresponds to the semicrystalline phase of carbon. Moreover, nitrogen doping causes a shift in the diffraction peak to a higher theta position, indicating the intercalation of nitrogen in NCD structures. The Raman spectra shown in Fig. 12d display the characteristic D and G bands of defective and graphitic phases in NCDs. The observed D and G bands at 1346 and 1585 cm^{-1}, respectively, are attributed to the disordered sp^3 and graphitic sp^2 domains of carbon atoms.[50] The high prominent ratio of the D and G bands indicates the semi-crystalline phase of carbon and the presence of tiny, disordered regions due to nitrogen doping. Additionally, photoluminescence Raman spectroscopy in Fig. 12e exhibits a prominent peak at 700 nm, confirming luminescence properties. This further enhances the potential of NCDs for various optical applications.[51]

Fig. 13a shows XPS full survey spectrum analysis confirming the presence of oxygen, carbon, and nitrogen in the NCD structure. The high-resolution C 1s XPS spectra (Fig. 13b) show three peaks centered at binding energies of 284.61, 285.55, and 287.41 eV, which correspond to the C=C, C=N, and C=O functional groups, respectively. The deconvoluted O 1s spectra (Fig. 13c) display three distinct peaks at binding energies of 532.20, 533.10, and 533.81 eV, corresponding to C=O, N–C=O, and O–C–O functional groups, respectively. These peaks

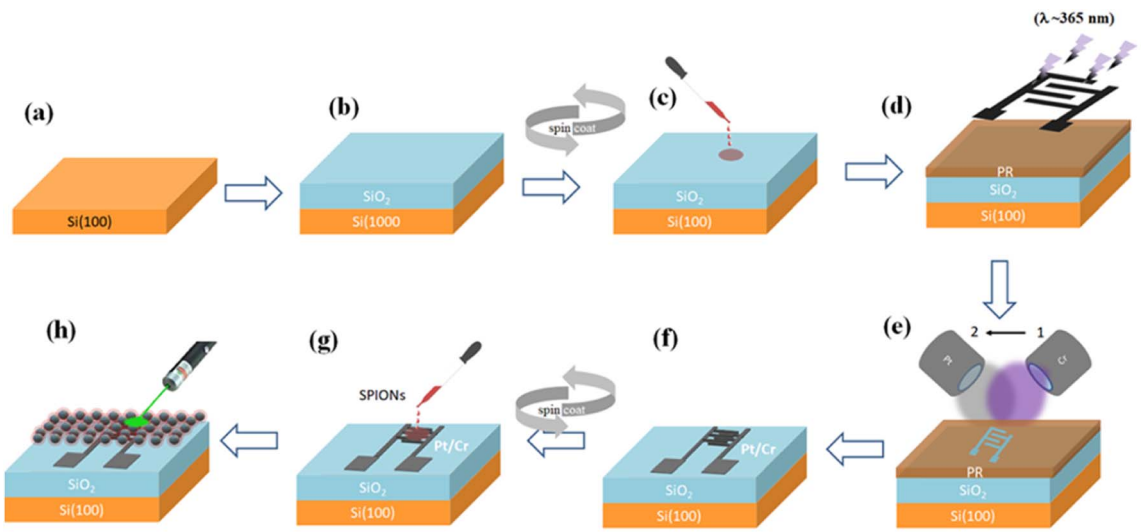

Scheme 2 Schematic process of the fabrication of noble metal-based μ-IDE device. (a) Deicing and cleaning of the wafer, (b) oxidation of Si (100) for a smooth buffer layer ~300 nm, (c) spin-coating of S-1813 PR with a thickness of ~1 μm followed by PAB at 110 °C, (d) patterning of PR using NUV photo exposure with I-365 nm, and (e) deposition of Pt/Cr over the patterned area. (f) lift-off process of PR and interdigitated electrode formation, (g) spin-coating of core–shell SPIONs, and (h) electrical characterization with monochromatic light illumination.

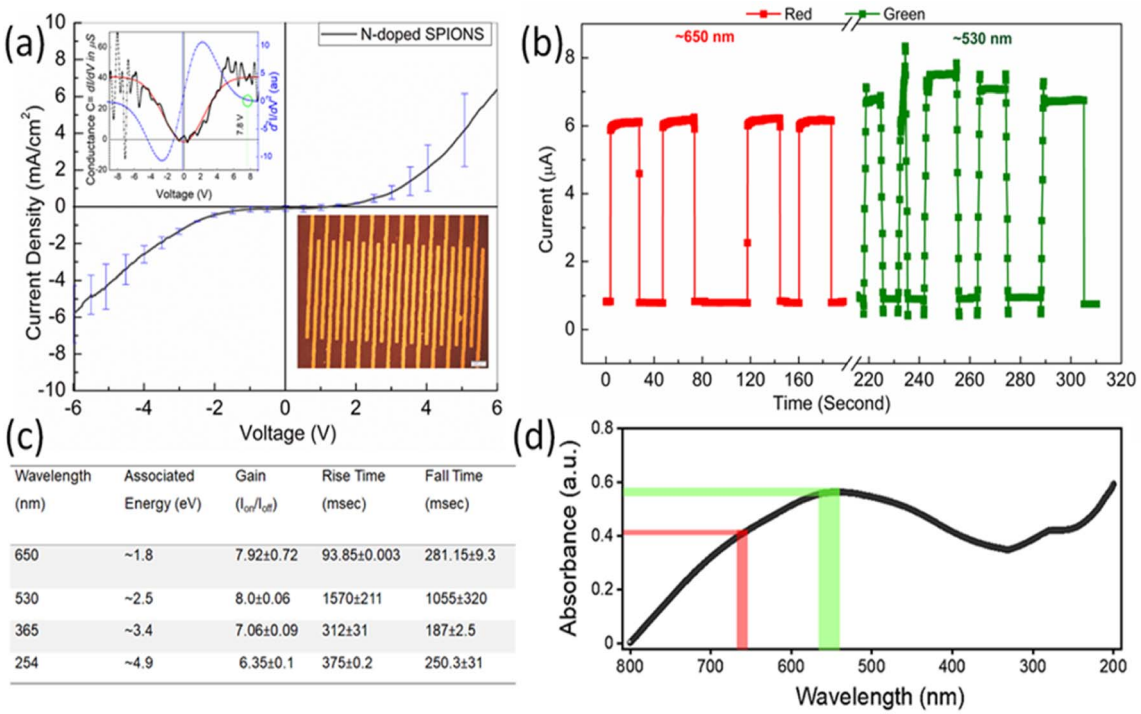

Wavelength (nm)	Associated Energy (eV)	Gain (I_{on}/I_{off})	Rise Time (msec)	Fall Time (msec)
650	~1.8	7.92±0.72	93.85±0.003	281.15±9.3
530	~2.5	8.0±0.06	1570±211	1055±320
365	~3.4	7.06±0.09	312±31	187±2.5
254	~4.9	6.35±0.1	375±0.2	250.3±31

Fig. 11 Electrical characteristics of the fabricated μ-IDE Pt/SPION heterostructure: (a) bias dependent current (*I*–*V*) characteristics for the 50 μm core–shell SPION channel; the inset shows the conductance d*I*/d*V* (inset left) for the abovementioned device structure; the optical image of μ-IDE Pt/SPIONs for electrical measurement (inset right); scale bar −500 μm. (b) Photo-response analysis under different wavelength illumination performed at 1 V bias. (c) Tabulated gain (I_{on}/I_{off}) for different illumination. (d) The UV-vis spectra of core–shell SPIONs in line with the photo-response; the large spectrum of absorption (700–250 nm) suggests the substantial number of carbons containing absorption sites responsive to distinct energy.

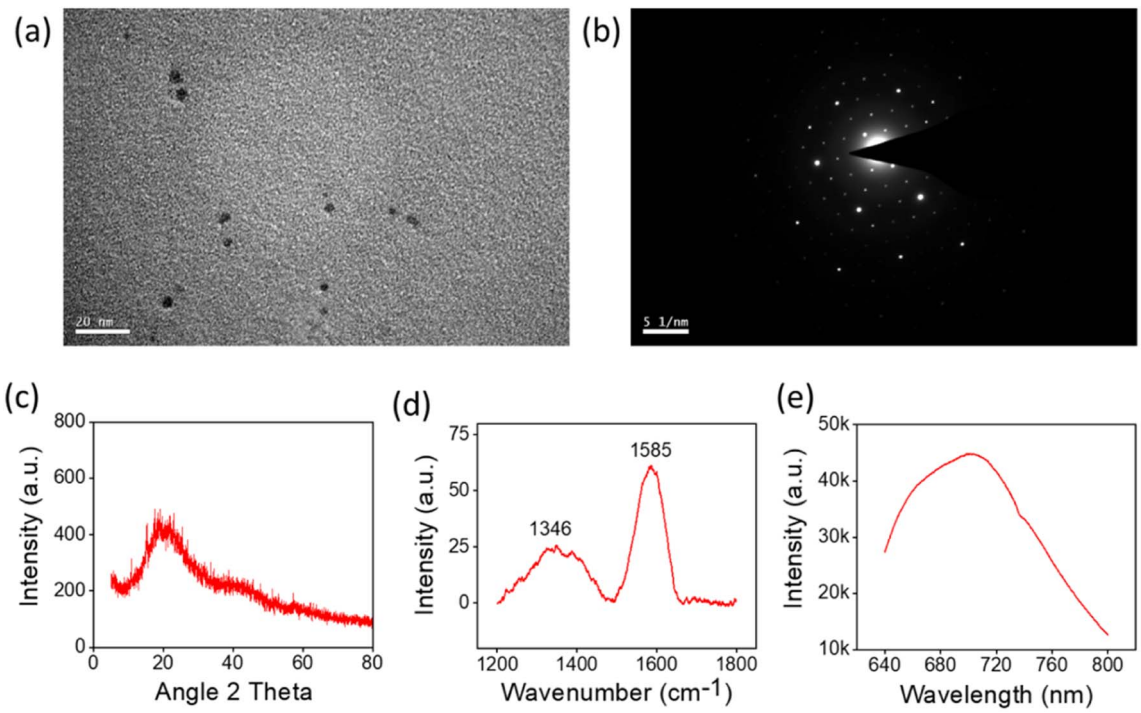

Fig. 12 (a) TEM image (scale bar: 20 nm), (b) SAED pattern (scale bar: 5^{-1} nm), (c) P-XRD spectra, (d) Raman spectra and (e) PL Raman spectra of NCDs, respectively.

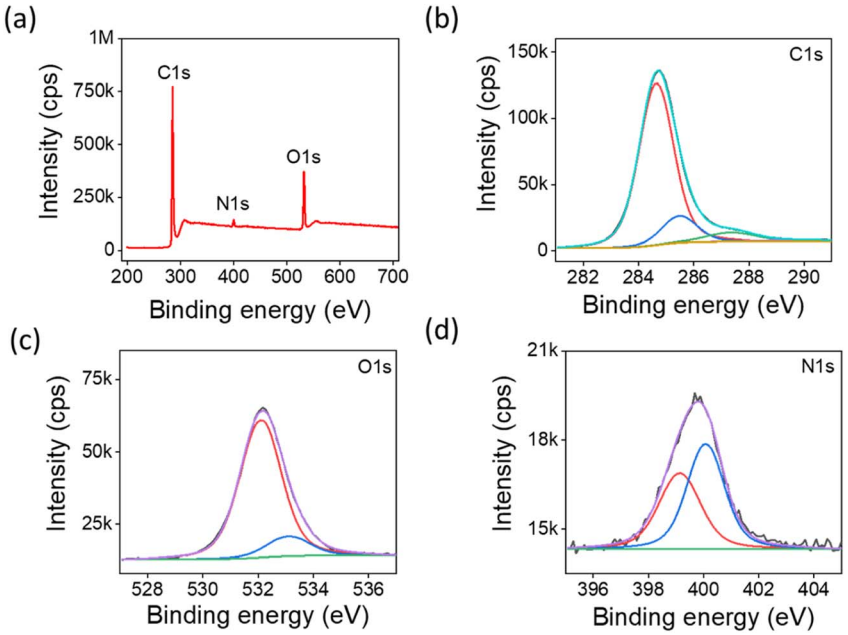

Fig. 13 Full survey (a) XPS spectra and high resolution deconvoluted XPS spectra of (b) carbon, (c) oxygen and (d) nitrogen in NCDs, respectively.

indicate the presence of carbonyl and carboxyl groups in the NCD structure. The high-resolution deconvoluted N 1s spectra (Fig. 13d) exhibit two peaks at binding energies of 399.10 and 400.10 eV, which may be attributed to the presence of C–NH and N–C=O functional species, respectively. These peaks indicate the presence of amino groups and nitrile or amide groups in the NCD structure. XPS results confirm the presence of abundant surface carbonyl and hydroxyl functional groups, as well as nitrogen doping in NCDs. These functional groups and nitrogen doping contribute to the unique optical properties and potential applications of NCDs.[52]

2.10 NCDs are biocompatible and display multicolor emission in confocal microscopy

Fig. 14a shows the band gap of NCDs, which was calculated to be 2.75 eV. This value falls within a broad visible region of the electromagnetic spectrum, validating the unique optical response of NCDs. Fluorescence spectra were used to characterize the excitation and emission behavior of NCDs, as shown in Fig. 14b and c. The excitation maximum was determined to be 400 nm, while the emission maximum was recorded at different excitation wavelengths and an excitation-dependent emission behavior was observed and confirmed multicolor emission.[28] The surface charge of NCDs was evaluated through zeta potential analysis studies. Fig. S6 in the ESI† shows measured surface charge to be

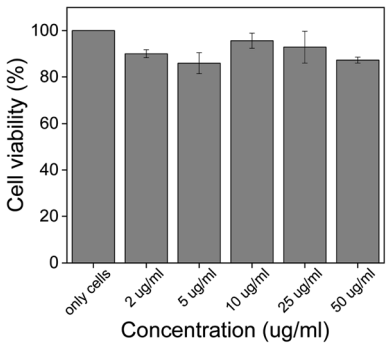

Fig. 15 Bar chart and error bars for percentage cell viability evaluated against HeLa cells and percentage cell viability for 24 hours (data are mean ± SD) (sample concertation = 0–50 μg ml^{-1}).

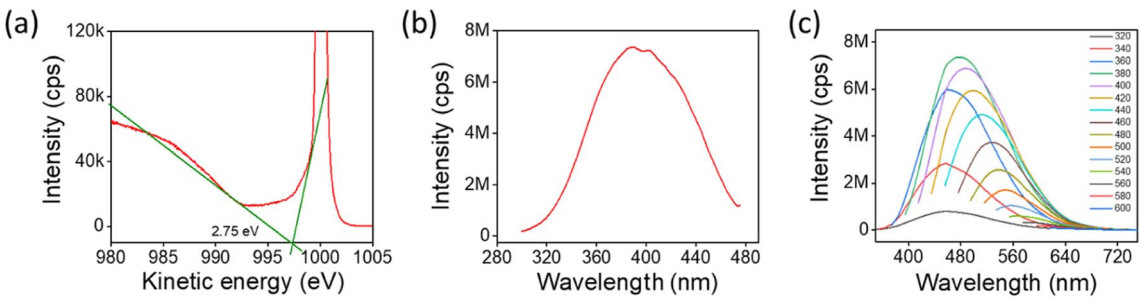

Fig. 14 (a) Band gap estimation, and (b) excitation and (c) emission spectra of NCDs, respectively.

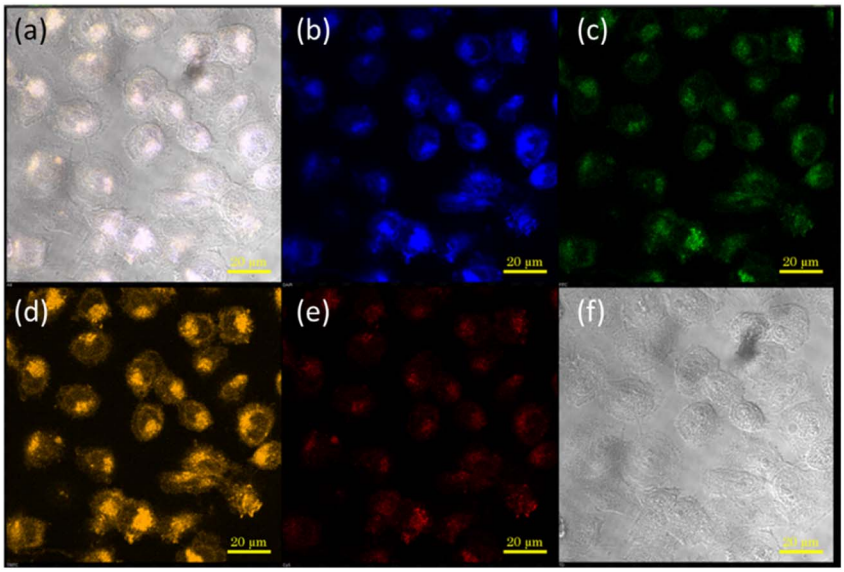

Fig. 16 Confocal laser scanning microscopy images of HeLa cells incubated with NCDs after an incubation time of 3 hours in a physiological medium. Figure represents (a) overlay image for all channels, (b) DAPI channel, (c) FITC channel, (d) TRITC channel, (e) CY5 channel, and (f) bright field image, respectively (DAPI – blue, FITC – green, TRITC – yellow and CY5 – red) (scale bar: 20 μm).

5.86 mV in a colloidal dispersion of the sample in an aqueous solution.

The cytotoxicity of NCDs was assessed using MTT assays against HeLa cells. The cell viability experiments were conducted using various concentrations of NCDs ranging from 0 to 50 μg ml^{-1}. The results of cell viability experiments after 24 hours are depicted in Fig. 15. The percentage cell viability was found to be over 80% even at higher concentrations. These cell viability results indicate that NCDs are biocompatible and have immense potential to be used in bioimaging.

We further studied cellular internalization of NCDs in HeLa cells. NCDs were incubated for 3 hours at a concentration of 10 μg ml^{-1} with HeLa cells and observed under a microscope. Fig. 16 shows confocal images in blue, green, yellow, and red emissions from cell cytoplasm indicating the uptake of NCDs. The excitation-dependent emission behavior observed in the cellular environment further confirms the ability of NCDs to emit light of distinct colors when illuminated at different wavelengths. Thus, the results suggest that NCDs could be used as an imaging agent in cellular internalization studies and fluorescence imaging techniques.

3 Conclusion

In this study, we introduce a revolutionary methodology for the production of two nanoscale goods, namely core–shell superparamagnetic iron oxide nanoparticles (SPIONs) and nitrogen doped carbon dots (NCDs). In particular, our technique incorporates a single-step synthesis process, which eliminates the need for any future modifications or separation and purification operations. The core–shell SPIONs revealed a variety of functions, including fluorescence and the capacity to emit several colours in confocal imaging. The individual particle magnetic susceptibility of core–shell SPIONs was measured, indicating considerably greater magnetic resonance contrast compared to commercially available contrast agents. The relaxivity value of the SPIONs was determined to be 156 mM^{-1} s^{-1}. The study showcased the biocompatibility of core–shell superparamagnetic iron oxide nanoparticles (SPIONs), as well as their proficient internalization into cancer cells. The results emphasize the potential of core–shell superparamagnetic iron oxide nanoparticles (SPIONs) in the area of targeted delivery. The photoresponsive devices based on μ-IDE-Pt/SPIONs exhibited rapid optical to current responsiveness and a substantial photo to dark current ratio. The study on photoinduced current investigated the rise and fall times of the device's reaction, which were found to be 93/281 milliseconds when exposed to a green laser. This discovery implies that the apparatus possesses considerable promise as a component for printed electronic health monitoring systems. On the other hand, nanocrystals (NCDs) have demonstrated a variety of advantageous attributes, such as multifunctionality, biocompatibility, multicolor emission, and substantial promise for implementation in biomedical cellular imaging. Furthermore, this study presents significant opportunities for further exploration into the single-step synthesis of nanoscale materials and the attainment of a substantial throughput yield during their production. The application of multifunctional core–shell SPIONs, as demonstrated in this research, may have substantial implications for the future advancement of interdigitated optoelectronic devices designed for health monitoring of humans.

Author contributions

A. T. conceived the study, performed the experiments, and wrote the manuscript. A. T. and J. K. R. conceptualized and supervised the study. All authors have given approval to the final

version of the manuscript. All authors reviewed the manuscript and provided feedback.

Conflicts of interest

The authors declare no competing financial interest.

Acknowledgements

The authors thank the Indian Institute of Technology Mandi for providing scientific facilities to perform the research work. The authors thank the Ministry of Education, Govt. of India, for funding the research work. The authors thank Dr R. K. Gupta from the Fortis Memorial Research Institute for the support in MR scanning. The authors thank Dr Anup Singh for the support in MR imaging. The authors thank Dr Satinder Sharma for the support in device fabrication and photocurrent measurements. The authors thank Dr Ayan Debnath for helping with MR imaging. The authors thank Dr Mohamad G. Moinuddin for helping with device fabrication and photocurrent measurements. The authors thank Dr Amir Mushtaq for helping with non-linear optical measurements. The authors thank Dr Ashutosh Singh for helping with bioimaging.

References

1 E. K. Lim, T. Kim, S. Paik, S. Haam, Y. M. Huh and K. Lee, *Chem. Rev.*, 2015, **115**, 327–394.
2 N. Lee, D. Yoo, D. Ling, M. H. Cho, T. Hyeon and J. Cheon, *Chem. Rev.*, 2015, **115**, 10637–10689.
3 Y. Lee, F. Koehler, T. Dillon, G. Loke, Y. Kim, J. Marion, M.-J. Antonini, I. Garwood, A. Sahasrabudhe, K. Nagao, X. Zhao, Y. Fink, E. T. Roche and P. Anikeeva, *Adv. Mater.*, 2023, 2301916.
4 N. Chekina, D. Horák, P. Jendelová, M. Trchová, M. J. Beneš, M. Hrubý, V. Herynek, K. Turnovcová and E. Syková, *J. Mater. Chem.*, 2011, **21**, 7630.
5 Y. Lu, B. He, J. Shen, J. Li, W. Yang and M. Yin, *Nanoscale*, 2015, **7**, 1606–1609.
6 S. K. Pahari, S. Olszakier, I. Kahn and L. Amirav, *Chem. Mater.*, 2018, **30**, 775–780.
7 O. Chen, L. Riedemann, F. Etoc, H. Herrmann, M. Coppey, M. Barch, C. T. Farrar, J. Zhao, O. T. Bruns, H. Wei, P. Guo, J. Cui, R. Jensen, Y. Chen, D. K. Harris, J. M. Cordero, Z. Wang, A. Jasanoff, D. Fukumura, R. Reimer, M. Dahan, R. K. Jain and M. G. Bawendi, *Nat. Commun.*, 2014, **5**, 5093.
8 M. Mahmoudi and M. A. Shokrgozar, *Chem. Commun.*, 2012, **48**, 3957.
9 A. Feld, J. P. Merkl, H. Kloust, S. Flessau, C. Schmidtke, C. Wolter, J. Ostermann, M. Kampferbeck, R. Eggers, A. Mews, T. Schotten and H. Weller, *Angew. Chem., Int. Ed.*, 2015, **54**, 12468–12471.
10 Y. Lu, B. He, J. Shen, J. Li, W. Yang and M. Yin, *Nanoscale*, 2015, **7**, 1606–1609.
11 Y. Lu, Y. Zheng, S. You, F. Wang, Z. Gao, J. Shen, W. Yang and M. Yin, *ACS Appl. Mater. Interfaces*, 2015, **7**, 5226–5232.
12 M. E. F. Brollo, R. López-Ruiz, D. Muraca, S. J. A. Figueroa, K. R. Pirota and M. Knobel, *Sci. Rep.*, 2014, **4**, 6839.
13 K. W. P. Orr, S. M. Collins, E. M. Reynolds, F. Nightingale, H. L. B. Boström, S. J. Cassidy, D. M. Dawson, S. E. Ashbrook, O. V. Magdysyuk, P. A. Midgley, A. L. Goodwin and H. H. M. Yeung, *Chem. Sci.*, 2021, **12**, 4494.
14 A. Tymoczko, M. Kamp, C. Rehbock, L. Kienle, E. Cattaruzza, S. Barcikowski and V. Amendola, *Nanoscale Horiz.*, 2019, **4**, 1326–1332.
15 Y. W. Lee, M. Kim, Z. H. Kim and S. W. Han, *J. Am. Chem. Soc.*, 2009, **131**, 17036–17037.
16 J. Lai, K. V. P. M. Shafi, A. Ulman, K. Loos, R. Popovitz-Biro, Y. Lee, T. Vogt and C. Estournès, *J. Am. Chem. Soc.*, 2005, **127**, 5730–5731.
17 G. F. Goya, T. S. Berquó, F. C. Fonseca and M. P. Morales, *J. Appl. Phys.*, 2003, **94**, 3520–3528.
18 J. Gao, H. Gu and B. Xu, *Acc. Chem. Res.*, 2009, **42**, 1097–1107.
19 H. Mamiya, H. Fukumoto, J. L. Cuya Huaman, K. Suzuki, H. Miyamura and J. Balachandran, *ACS Nano*, 2020, **14**, 8421–8432.
20 X. Xu, H. Xiang, Z. Wang, C. Wu and C. Lu, *J. Alloys Compd.*, 2022, **923**, 166459.
21 S. S. Laha, N. D. Thorat, G. Singh, C. I. Sathish, J. Yi, A. Dixit and A. Vinu, *Small*, 2022, **18**, 2104855.
22 C. I. M. Santos, I. F. A. Mariz, S. N. Pinto, G. Gonçalves, I. Bdikin, P. A. A. P. Marques, M. G. P. M. S. Neves, J. M. G. Martinho and E. M. S. Maçôas, *Nanoscale*, 2018, **10**, 12505–12514.
23 P. Lesani, A. H. Mohamad Hadi, Z. Lu, S. Palomba, E. J. New and H. Zreiqat, *Commun. Mater.*, 2021, **2**(1), 1–12.
24 Y. Bai, J. Zhao, S. Wang, T. Lin, F. Ye and S. Zhao, *ACS Appl. Mater. Interfaces*, 2021, **13**, 35365–35375.
25 J. Zheng, Z. Cao, M. Lei, Z. Nie, Y. Yang, X. Liu and B. Xu, *J. Mater. Chem. C*, 2023, **11**, 3342–3353.
26 Y. Ma, C. Zhang, G. Ji and J. Y. Lee, *J. Mater. Chem.*, 2012, **22**, 7845–7850.
27 G. A. Gebreslase, D. Sebastián, M. V. Martínez-Huerta and M. J. Lázaro, *J. Electroanal. Chem.*, 2022, **925**, 116887.
28 D. Sengottuvelu, A. K. Shaik, S. Mishra, H. Ahmad, M. Abbaszadeh, N. I. Hammer and S. Kundu, *ACS Omega*, 2022, **7**, 27742–27754.
29 D. Shen, M. Xiao, X. Zhao, Y. Xiao, W. W. Duley and Y. N. Zhou, *ACS Appl. Mater. Interfaces*, 2021, **13**, 34266–34273.
30 X. Wang, W. Jin, Z. Chang and K. S. Chiang, *Opt. Lett.*, 2019, **44**, 1480–1483.
31 B. Kang, Y. Kim, W. J. Yoo and C. Lee, *Small*, 2018, **14**, 1802593.
32 A. Tiwari, N. C. Verma, A. Singh, C. K. Nandi and J. K. Randhawa, *Nanoscale*, 2018, **10**, 10389–10394.
33 A. Tiwari, N. C. Verma, S. Turkkan, A. Debnath, A. Singh, G. Draeger, C. K. Nandi and J. K. Randhawa, *ACS Appl. Nano Mater.*, 2020, **3**, 896–904.
34 A. Tiwari, A. Singh, A. Debnath, A. Kaul, N. Garg, R. Mathur, A. Singh and J. K. Randhawa, *ACS Appl. Nano Mater.*, 2019, **2**, 3060–3072.

35 A. Tiwari, N. C. Verma, J. K. Randhawa and C. K. Nandi, *J. Phys. Chem. C*, 2019, **123**, 27759–27764.
36 A. Tiwari, P. Bhatiya and J. K. Randhawa, *Dalton Trans.*, 2020, **49**, 12380–12389.
37 A. Tiwari, R. Kumar, O. Shefi and J. K. Randhawa, *ACS Appl. Bio Mater.*, 2020, **3**, 4665–4673.
38 M. Sun, B. Sun, Y. Liu, Q.-D. Shen and S. Jiang, *Sci. Rep.*, 2016, **6**, 22368.
39 A. B. Bourlinos, A. Stassinopoulos, D. Anglos, R. Zboril, V. Georgakilas and E. P. Giannelis, *Chem. Mater.*, 2008, **20**, 4539–4541.
40 X. Meng, Q. Chang, C. Xue, J. Yang and S. Hu, *Chem. Commun.*, 2017, **53**, 3074–3077.
41 J. Gao, G. Liang, J. S. Cheung, Y. Pan, Y. Kuang, F. Zhao, B. Zhang, X. Zhang, E. X. Wu and B. Xu, *J. Am. Chem. Soc.*, 2008, **130**, 11828–11833.
42 H. Wei, O. T. Bruns, M. G. Kaul, E. C. Hansen, M. Barch, A. Wiśniowska, O. Chen, Y. Chen, N. Li, S. Okada, J. M. Cordero, M. Heine, C. T. Farrar, D. M. Montana, G. Adam, H. Ittrich, A. Jasanoff, P. Nielsen and M. G. Bawendi, *Proc. Natl. Acad. Sci. U. S. A.*, 2017, **114**, 2325–2330.
43 S. Sievers, K. F. Braun, D. Eberbeck, S. Gustafsson, E. Olsson, H. W. Schumacher and U. Siegner, *Small*, 2012, **8**, 2675–2679.
44 L. Angeloni, D. Passeri, S. Corsetti, D. Peddis, D. Mantovani and M. Rossi, *Nanoscale*, 2017, **9**, 18000–18011.
45 J. Sifford, K. J. Walsh, S. Tong, G. Bao and G. Agarwal, *Nanoscale Adv.*, 2019, **1**, 2348.
46 C. Liu, Y. Zheng, B. Zhang, X. Zheng, S. Hu and K. Han, *IEEE Access*, 2019, **7**, 50536–50548.
47 S. Hwang, C. N. LaFratta, V. Agarwal, X. Yu, D. R. Walt and S. Sonkusale, *IEEE Sens. J.*, 2009, **9**, 609–615.
48 N. Lovecchio, F. Costantini, E. Parisi, M. Nardecchia, M. Tucci, A. Nascetti, G. de Cesare and D. Caputo, *IEEE Trans. Biomed. Circuits Syst.*, 2018, **12**, 1337–1344.
49 V. Hinterberger, C. Damm, P. Haines, D. M. Guldi and W. Peukert, *Nanoscale*, 2019, **11**, 8464–8474.
50 H. Li, Z. Kang, Y. Liu and S. T. Lee, *J. Mater. Chem.*, 2012, **22**, 24230–24253.
51 Y. Dong, H. Pang, H. Bin Yang, C. Guo, J. Shao, Y. Chi, C. M. Li and T. Yu, *Angew. Chem., Int. Ed.*, 2013, **52**, 7800–7804.
52 Z. Yang, M. Xu, Y. Liu, F. He, F. Gao, Y. Su, H. Wei and Y. Zhang, *Nanoscale*, 2014, **6**, 1890–1895.